ELSEVIER

Journal of Fluids and Structures 24 (2008) 799–818

JOURNAL OF FLUIDS AND STRUCTURES

www.elsevier.com/locate/jfs

Fluid–structure interaction analysis of flexible composite marine propellers

Y.L. Young*

Department of Civil and Environmental Engineering, Princeton University, Princeton, NJ 08544, USA

Received 1 December 2006; accepted 22 December 2007
Available online 18 March 2008

Abstract

There is an increasing interest in the marine industry to use composites to improve the hydrodynamic and structural performance of naval structures. Composite materials have high strength-to-weight and stiffness-to-weight ratios, and the fiber orientations can be exploited to tailor the structural deformation to reduce the load and stress variations by automatically adjusting the shape of the structure. For marine propellers, the bending–twisting coupling characteristics of anisotropic composites can be exploited to passively tailor the blade rake, skew, and pitch distributions to improve propeller performance. To fully explore the advantages of composite marine propellers, a coupled boundary element (BEM) and finite element (FEM) approach is presented to study the fluid–structure interaction of flexible composite propellers in subcavitating and cavitating flows. An overview of the formulation for both the fluid and structural models is presented. Experimental validation studies are shown for two composite propellers tested at the Naval Surface Warfare Center (NSWCCD). The feasibility of passive hydroelastic tailoring of composite marine propellers is discussed.
Published by Elsevier Ltd.

Keywords: Fluid–structure interaction; Composite; Hydroelastic; Propeller

1. Introduction

Traditionally, marine propellers are made of manganese–nickel–aluminum–bronze (MAB) or nickel–aluminum–bronze (NAB) for their superior corrosion resistance, high-yield strength, reliability, and affordability. However, it is expensive to machine metallic materials into complex propeller geometries. Moreover, metallic propellers are subject to corrosion and cavitation damage, fatigue-induced cracking, and have relatively poor acoustic damping properties that can lead to noise due to structural vibration (Mouritz et al., 2001). Thus, there is an increased interest in the use of composites as alternate materials. Composite materials have high-strength-to-weight and stiffness-to-weight ratios, which can lead to substantial weight savings. The use of lighter composite materials also means the blades can be made thicker and more flexible to improve the hydrodynamic performance by increasing the cavitation inception speeds. Moreover, composites can offer the potential benefits of reduced corrosion and cavitation damage, improved fatigue performance, lower noise, improved material damping properties, and reduced lifetime maintenance cost. In addition,

*Tel.: +1 609 258 5426; fax: +1 609 258 1563.
E-mail address: yyoung@princeton.edu

0889-9746/$ - see front matter Published by Elsevier Ltd.
doi:10.1016/j.jfluidstructs.2007.12.010

the load-bearing fibers can be aligned and stacked to reduce fluttering and to improve the hydrodynamic efficiency by automatically adjusting the shape of the blade.

According to Mouritz et al. (2001), the first use of composite marine propellers was on Soviet fishing boats in the 1960s. Later, the USSR conducted extensive sea trials to compare the performance of 0.25 m to 3 m diameter composite and metal propellers with the same geometry on commercial ships with displacements of 2–5000 tons traveling at speeds of 5–35 knots (Ashkenazi et al., 1974). The performance between composite and metal propellers was virtually equal in terms of speed, fuel consumption, engine workload, absorbed horsepower and operating life; but the composite propellers reduced the engine and shaft vibrations by approximately 25%, and resulted in less noise and hull vibration (Ashkenazi et al., 1974). Performance tests of composite propellers were also conducted on a range of naval vessels (including landing craft, minesweepers, torpedoes, small boats, and tri-marans) since the 1980s, but much of the scientific information is not available in the open literature (Mouritz et al., 2001). Based on the limited information given in public literature (Pegg and Reyes, 1987; Womack, 1993; Kane and Dow, 1994; Searle and Shot, 1994; Anon, 2002), the hydrodynamic performance of composite propellers is approximately the same as their metallic counterparts. However, they offer the added benefits of weight reduction (between 50% and 80%), lowered production costs (by approximately 60–70%), smoother take-up of power, reduced noise, reduced blade vibration, better cavitation erosion resistance, and better fatigue performance. Except for a few cases, most of these composite propellers were designed to be the same as their metallic counterparts. Thus, the benefits of hydroelastic tailoring have not been exploited. The anisotropic characteristics of laminated fiber composites allow 3-D passive tailoring of the blade deformation, which is not possible for metallic propellers. Composites can be exploited to reduce the load and stress variations transmitted to the shaft by automatically adjusting the pitch, rake, and skew distributions in spatially varying flows. However, despite these potential benefits of composites, they are not widely used in marine vessels. This is in part due to the dependence on reliable, consistent, and cost-effective manufacturing techniques to achieve the designed material properties and characteristics, which were not available in the past. Another important factor is the lack of design rules, a large systematic empirical database, or reliable simulation/design tools.

1.1. Previous work

One of the early numerical models developed for the analysis of a 3-D composite marine propeller was presented in Lin (1991a, b). Stress calculations were compared for a composite marine propeller and a geometrically identical isotropic NAB propeller. The composite blade was constructed of multiple layers of braided fiber in a thick-shell skin over a foam-filled core with shear-webs as internal support. The fluid pressure and centrifugal loads were considered using PSF-2, a non-cavitating vortex-lattice method (VLM) developed by Kerwin and Lee (1978) and Greeley and Kerwin (1982). The stress analysis was performed using the commercial finite element (FEM) software ABAQUS. The effective modulus method was applied and 3-D quadratic solid elements were used for the FEM model. Compared to the NAB propeller, the composite propeller produced an order of magnitude higher elastic deformation at the tip and approximately 50% higher in-plane bending and shearing stresses (Lin, 1991a, b). However, the assumed material modulus of the composite was very low in Lin's model. Laboratory and sea trials of composite propellers generally experience smaller tip deflections due to the use of much stiffer carbon fiber composites (Mouritz et al., 2001).

In Lin and Lin (1996), a coupled 3-D FEM/VLM (PSF-2) method was presented for the hydroelastic analysis of marine propellers. The effect of geometric nonlinearities was considered. The source strengths of the VLM were expressed in terms of the unknown blade displacements, and the hydrodynamic excitation force vector for the FEM was expressed in terms of the unknown vortex strengths. The fluid and solid governing equations were fully coupled, and were solved using a Newton–Raphson procedure. A 3-D degenerated shell elements with five degrees of freedom at each node were applied. The method was able to determine the hydroelastic behavior of composite marine propellers in steady, subcavitating flows. The coupled 3-D FEM/VLM procedure was applied by Lin and Lin (1997) to assess the effects of stacking sequence on the hydroelastic behavior of composite propeller blades. They concluded that the stacking sequence influenced the thrust, pitch, and camber of the composite blades, especially in the low-advance coefficient regions. In Lee and Lin (2004) and Lin and Lee (2004), a genetic algorithm was added to the coupled FEM/VLM procedure to determine the optimal stacking sequence of the fiber composites. Most recently, a 3-D stress evaluation procedure and the Hashin material failure criterion (Hashin, 1980) were added to the coupled FEM/VLM method for strength evaluation of composite marine propellers (Lin and Lin, 2005). The 3-D equilibrium equations were employed to resolve the transverse shear stresses. The least squares method was applied to smooth the stress distributions. The results indicated that composite blades might be subject to matrix tension and delamination failures depending on the flow condition and stacking sequence.

1.2. Objective

All of the above-mentioned methods are limited to marine propellers operating in steady, subcavitating flow. However, marine propellers usually operate in a spatially varying wake. In addition, blade surface cavitation is expected at speeds above 13−15 m/s (25–30 knots). Thus, it is crucial to be able to investigate the dynamic performance of flexible composite propellers in subcavitating and cavitating conditions. Moreover, knowledge of the dynamic characteristics of composite propellers is needed in order to avoid resonant blade vibration or fatigue problems. The objective of this work is to improve the understanding of, and predictive capabilities for, the hydroelastic behavior of flexible composite propellers in subcavitating and cavitating flows. To achieve this objective, a general analysis methodology is presented for a flexible composite marine propeller subject to hydrodynamic and inertial loads, including the effect of unsteady cavitation.

2. Mathematical model

To analyze the cavitation pattern, loading and response of high-speed marine propellers, a 3-D boundary element method (BEM) developed by the author and the hydrodynamic group at The University of Texas at Austin is coupled with the commercial finite element (FEM) software ABAQUS (ABAQUS, 2004). Compared to VLMs, which discretize the mean camber surface, the BEM can better capture the flow details because it inherently accounts for the effect of thickness loading coupling by discretizing the actual blade surface. Moreover, the developed BEM is able to account for the effects of flow unsteadiness, complex cavitation or ventilation patterns, non-zero blade trailing edge thickness, and varying blade submergence, all of which are important in order to fully explore the potential advantage of composite propellers in a wide range of operating conditions.

In the sections that follow, an overview of the fluid–structure interaction model is presented. To limit the length of this paper, only the key governing equations and boundary conditions are presented. Details of the fluid model and associated validation studies can be found in Kinnas and Fine (1992), Young and Kinnas (2001, 2003a, b, 2004) and Kinnas and Young (2003). Details of the fluid–structure interaction model and validation studies for metallic marine propellers with small deformations can be found in Young (2007). In this work, the method is extended to model fluid–structure interaction of flexible composite propellers with large deformations.

2.1. General formulation

A moving body in a steady flow field is equivalent to that of a stationary body in moving flow field. Hence, the problem of a marine propeller advancing forward with a constant velocity V_a can be solved by considering the propeller to be fixed in a spatial location but subject to a moving inflow. Due to the presence of the hull and other nearby boundaries (e.g. shaft, rudder, free surface, etc.), the spatial distribution of the inflow $\mathbf{V}_e(x_s, y_s, z_s)$ may be non-uniform. Here, (x_s, y_s, z_s) is the right-handed Cartesian ship-fixed coordinates system with the origin located at the center of the hub. The x_s-axis is co-linear with the propeller axis of rotation and is positive in the downstream direction. The y_s-axis is positive in the direction opposite to gravity.

To solve the problem using BEM (potential theory), the inflow velocity, $\mathbf{V}_e(x_s, y_s, z_s)$, is assumed to be the *effective* wake; i.e. the total velocity minus the propeller-induced velocity by potential flow theory. In other words, $\mathbf{V}_e(x_s, y_s, z_s)$ is the sum of the *nominal* inflow in the absence of the propeller and the vortical interaction between the propeller and the inflow. $\mathbf{V}_e$ can be obtained by iterating between a potential (incompressible, inviscid, irrotational) solver and an Euler (incompressible and inviscid) solver (Kinnas et al., 2000; Choi, 2000).

The propeller is assumed to be rotating at a constant angular velocity ω. To avoid the need for a moving mesh, the fluid problem is solved using a rotating blade-fixed coordinate system (x, y, z), which is attached to the reference blade. As shown in Fig. 1, the x-axis is the same as the x_s-axis, and the y-axis is co-linear with the pitch change axis with the positive direction pointing toward the blade tip. The inflow velocity, $\mathbf{V}_{\text{in}}$, at a given location in the blade-fixed coordinate system, $\mathbf{x} = (x, y, z)$, at time t can be expressed as follows:

$$\mathbf{V}_{\text{in}}(\mathbf{x}, t) = \mathbf{V}_e(x_s, r_s, \theta_s) - \mathbf{\Omega} \times \mathbf{x}, \tag{1}$$

where $r_s = \sqrt{y_s^2 + z_s^2} = \sqrt{y^2 + z^2}$, $\theta_s = \arctan(z_s/y_s) = \theta - \omega t$, $\theta = \arctan(z/y)$, and $\mathbf{\Omega} = [-\omega,\ 0,\ 0]^{\text{T}}$.

From here on, the notation $(\mathbf{x}, t)$ will be dropped for simplicity since both the fluid and solid problems are solved with respect to the blade-fixed coordinate system.

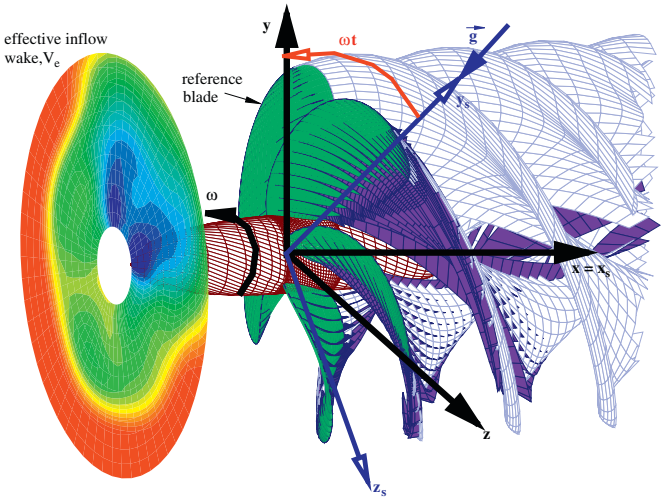

Fig. 1. Propeller subjected to a general inflow wake. The propeller-fixed coordinate system which rotates with the propeller (x, y, z) and the ship-fixed (inertial) coordinate system (x_s, y_s, z_s) are shown.

The total velocity $\mathbf{V}_t$ with respect to the blade-fixed system can be written as

$$\mathbf{V}_t = \mathbf{V}_{\text{in}} + \nabla\Phi, \tag{2}$$

where Φ is the perturbation velocity potential corresponding to the propeller-induced flow field.

The inviscid, incompressible momentum equation with respect to the rotating blade-fixed coordinate system can be expressed as follows:

$$\frac{D\mathbf{V}_t}{Dt} = \frac{\partial \mathbf{V}_t}{\partial t} + (\mathbf{V}_t \cdot \nabla)\mathbf{V}_t = -\nabla\left(\frac{P}{\rho}\right) + \mathbf{g} - \boldsymbol{\Omega} \times (\boldsymbol{\Omega} \times \mathbf{x}) - 2\boldsymbol{\Omega} \times \mathbf{V}_t, \tag{3}$$

where the last two terms in Eq. (3) denote the centrifugal acceleration and Coriolis acceleration, respectively.

Applying the continuity equation $(\nabla \cdot \mathbf{V}_t = 0)$ along with Eqs. (1) and (2), and assuming $\partial \mathbf{V}_e/\partial t = 0$ (steady effective wake), integration of Eq. (3) between two points on the same streamline yields the following equation for the absolute total pressure P (Young, 2007):

$$P - P_o = \rho\left[\frac{1}{2}|\mathbf{V}_{\text{in}}|^2 - \frac{\partial \Phi}{\partial t} - \frac{1}{2}|\mathbf{V}_t|^2\right], \tag{4}$$

where $P_o = P_{\text{atm}} + \rho g d_s$ is the absolute hydrostatic pressure at $\mathbf{x}$; P_{atm} is the atmospheric pressure and d_s is the submerged depth of point $\mathbf{x}$ from the free surface; ρ and g are the fluid density and amplitude of the gravitational acceleration, respectively.

In the blade-fixed coordinate system, the discrete equation of motion for the blade can be written as follows:

$$[\mathbf{M}]\{\ddot{\mathbf{u}}\} + [\mathbf{C}]\{\dot{\mathbf{u}}\} + [\mathbf{K}]\{\mathbf{u}\} = \{\mathbf{F}_{ce}\} + \{\mathbf{F}_{co}\} + \{\mathbf{F}_h\}, \tag{5}$$

where $\{\ddot{\mathbf{u}}\}$, $\{\dot{\mathbf{u}}\}$, and $\{\mathbf{u}\}$ are the local nodal acceleration, velocity, and displacement vectors, respectively. $[\mathbf{M}] = \int \rho_s[\mathbf{N}]^{\mathrm{T}}[\mathbf{N}]\,\mathrm{d}V$, $[\mathbf{C}] = \int c[\mathbf{N}]^{\mathrm{T}}[\mathbf{N}]\,\mathrm{d}V$, and $[\mathbf{K}] = \int[\mathbf{B}]^{\mathrm{T}}[\mathbf{D}][\mathbf{B}]\,\mathrm{d}V$ are the consistent global mass, damping, and stiffness matrices, respectively. $[\mathbf{N}]$, $[\mathbf{B}] = \partial[\mathbf{N}]$, and $[\mathbf{D}]$ are the displacement interpolation matrix, strain–displacement matrix, and material constitutive matrix, respectively. The variables ρ_s and c denote the mass density and frequency-independent mass damping of the blade, respectively.

The nodal force vectors on the right-hand side of Eq. (5) denote the centrifugal force $(\{\mathbf{F}_{ce}\} = \int \rho_s[\mathbf{N}]^{\mathrm{T}}\{\mathbf{f}_{ce}\}\,\mathrm{d}V)$, Coriolis force $(\{\mathbf{F}_{co}\} = \int \rho_s[\mathbf{N}]^{\mathrm{T}}\{\mathbf{f}_{co}\}\,\mathrm{d}V)$, and the hydrodynamic force $(\{\mathbf{F}_h\} = \int[\mathbf{N}]^{\mathrm{T}}\{\mathbf{P}\}\,\mathrm{d}S)$, respectively, where

$$\mathbf{f}_{ce} = -\boldsymbol{\Omega} \times (\boldsymbol{\Omega} \times (\mathbf{x} + \mathbf{u})), \quad \mathbf{f}_{co} = -2\boldsymbol{\Omega} \times \dot{\mathbf{u}}. \tag{6,7}$$

2.2. Fluid–structure interaction

To account for the effect of fluid–structure interaction, the propeller-induced perturbation potential, Φ, is decomposed into a part due to large rigid-blade rotation ϕ and a part due to small elastic blade deformation φ:

$$\Phi = \phi + \varphi. \tag{8}$$

Similarly, the total pressure P, can also be decomposed into two parts (Young, 2007):

$$P = P_r + P_v, \tag{9}$$

$$P_r = P_o + \rho\left[\frac{1}{2}|\mathbf{V}_{\text{in}}|^2 - \frac{\partial\phi}{\partial t} - \frac{1}{2}|\mathbf{V}_{tr}|^2\right], \tag{10}$$

$$P_v = \rho\left[-\frac{\partial\varphi}{\partial t} - \mathbf{V}_{\text{in}}\cdot\nabla\varphi\right], \tag{11}$$

where P_r and P_v are the hydrodynamic pressure due to rigid-blade rotation and elastic blade deformation, respectively. $\mathbf{V}_{tr} = \mathbf{V}_{\text{in}} + \nabla\phi$ is the total velocity without considering the effect of elastic blade deformation.

It should be noted here that the effect of large blade deformation is considered by iterating between the BEM and FEM solvers and by updating the BEM geometry using the deformations calculated from the FEM solver. Additional details about the solution procedure are given in Section 2.4.

In this work, a low-order BEM is used to solve the boundary-value problems for ϕ and φ.

(i) Rigid-blade problem for ϕ:

$$\nabla^2\phi = 0 \quad \text{in fluid domain } \Gamma_F, \tag{12}$$

$$\frac{\partial\phi}{\partial n} = -\mathbf{V}_{\text{in}}\cdot\mathbf{n} \quad \text{on wetted blade and hub surfaces } S_{WB}, \tag{13}$$

$$P_r = P_c \quad \text{on cavity surfaces } S_C, \tag{14}$$

$$P_r^+ = P_r^- \quad \text{on wake surfaces } S_W, \tag{15}$$

$$\nabla\phi = 0 \quad \text{at infinity } S_\infty, \tag{16}$$

$$\frac{D}{Dt}(n-h) = 0 \quad \text{on cavity surfaces } S_{CB}\cup S_{CW}, \tag{17}$$

$$h_{TE} = 0 \quad \text{at cavity trailing edge}, \tag{18}$$

$$P_r > P_c \quad \text{on wetted blade surfaces } S_{WB}, \tag{19}$$

$$h_{LE} \geqslant 0 \quad \text{at cavity leading edge}, \tag{20}$$

where $\mathbf{n}$ is the outward unit normal vector. P_c is the saturated vapor pressure of the liquid; h is the thickness of the cavity defined in the normal n direction, and h_{TE} and h_{LE} are the thicknesses of the cavity trailing edge and leading edge, respectively. The superscripts "+" and "−" denote the upper and lower wake surfaces, respectively.

For a given cavitation number ($\sigma_n \equiv (P_o - P_c)/\frac{1}{2}\rho n^2 D^2$), where n is the propeller rotational frequency and D is the propeller diameter, and a given initial guess of cavity detachment location and cavity length, Eqs. (12)–(16) to formulate a mixed boundary-value problem for ϕ. Eq. (12) can be uniquely solved using BEM by applying Green's third identity subject to the flow tangency (free slip) boundary condition (Eq. (13)), constant cavity pressure condition (Eq. (14)), zero-force wake condition (Eq. (15)), and infinity condition (Eq. (16)). Eq. (17) is the flow tangency condition on the cavity surface, and is used to determine the cavity thickness h, defined normal to the blade surface. To determine the correct extent of the cavities, a Newton–Raphson algorithm is applied until the cavity closure condition, Eq. (18), is satisfied everywhere on the blade at each blade position. The cavity detachment locations are also determined in an iterative manner by satisfying the Villat–Brillouin smooth detachment condition (Brillouin, 1911; Villat, 1914), which can be expressed in the form of Eqs. (19) and (20). A *split* panel technique (Kinnas and Fine, 1993) is used to treat blade surface panels intersected by the cavity trailing edge. To save computational time, the solution at each time step (blade angle increment) is obtained only for the reference blade. The influence of each of the other blades is accounted for in a progressive manner by using the solution from an earlier time step when the reference blade was in the position of that blade. Once the values of ϕ are known on all the blade panels at each time step, the rigid-blade component of the hydrodynamic pressure, P_r, can be computed using Eq. (10), which is then imposed as normal tractions on the blade surface in the FEM model.

(ii) Elastic blade problem for φ:

$$\nabla^2\varphi = 0 \quad \text{in fluid domain } \Gamma_F, \tag{21}$$

$$\frac{\partial \varphi}{\partial n} = \dot{\delta}_n \quad \text{on the blade surface } S_B, \tag{22}$$

$$P_v^+ = P_v^- \quad \text{on wake surfaces } S_W, \tag{23}$$

$$\nabla \varphi = 0 \quad \text{at infinity } S_\infty, \tag{24}$$

where $\dot{\delta}_n$ is the normal component of the Lagrangian solid body velocity vector at the centroid of the BEM panel. The boundary conditions represented in Eqs. (22)–(24) denote the flow tangency condition at the deformable blade surface, the zero-force wake condition, and the infinity condition, respectively.

Similar to the rigid-blade problem, Eq. (21) can be solved using BEM by applying Green's third identity. For simplicity, the solution to Green's third identity can be expressed in matrix form as follows:

$$\{\varphi\} = [\mathbf{H}]\{\dot{\delta}_n\} = [\mathbf{H}][\mathbf{T}]\{\dot{\mathbf{u}}\}, \tag{25}$$

where $[\mathbf{H}]$ is the combined BEM influence coefficient matrix for the induced potential, and $[\mathbf{T}]$ is the transformation matrix which maps the vector of FEM nodal velocities $\{\dot{\mathbf{u}}\}$ to the vector of normal velocities at the centroid of the BEM panels $\{\dot{\delta}_n\}$.

Hence, the inertial and dissipative hydrodynamic force due to elastic blade motion, $\{\mathbf{F}_{hv}\}$, can be written as follows (Young, 2007):

$$\{\mathbf{F}_{hv}\} = \int [\mathbf{N}]^{\mathrm{T}}\{\mathbf{P}_{\mathbf{v}}\}\mathrm{d}S = -[\mathbf{M}_H]\{\ddot{\mathbf{u}}\} - [\mathbf{C}_H]\{\dot{\mathbf{u}}\}, \tag{26}$$

where $[\mathbf{M}_H]$ is the hydrodynamic added mass matrix, and $[\mathbf{C}_H]$ is the hydrodynamic damping matrix:

$$[\mathbf{M}_H] = \rho \int [\mathbf{N}]^{\mathrm{T}}[\mathbf{H}][\mathbf{T}]\,\mathrm{d}S, \tag{27}$$

$$[\mathbf{C}_H] = \rho \int [\mathbf{N}]^{\mathrm{T}}[\mathbf{V}_{in} \cdot \nabla \mathbf{H}][\mathbf{T}]\,\mathrm{d}S. \tag{28}$$

2.3. FEM model

The discrete equation of motion, Eq. (5), in the blade-fixed coordinate system can be rewritten as

$$([\mathbf{M}] + [\mathbf{M}_H])\{\ddot{\mathbf{u}}\} + ([\mathbf{C}] + [\mathbf{C}_H])\{\dot{\mathbf{u}}\} + [\mathbf{K}]\{\mathbf{u}\} = \{\mathbf{F}_{ce}\} + \{\mathbf{F}_{co}\} + \int [\mathbf{N}]^{\mathrm{T}}\{\mathbf{P}_{\mathbf{r}}\}\mathrm{d}S, \tag{29}$$

which is solved using the commercial FEM software ABAQUS/Standard (ABAQUS, 2004).

In the FEM model, the blade is assumed to be made of linear elastic, orthotropic carbon fiber laminates stacked in the thickness direction, and is modeled by stacking 3-D quadrilateral solid elements in the thickness direction. A schematic drawing of the different layering configurations that can be considered by the current coupled BEM–FEM solver, along with the definition of the fiber direction with respect to the local spanwise coordinate, and stress–strain relation for a linear elastic, orthotropic material are shown in Fig. 2. All the nodes at the root of the blade are fixed, i.e. the blade is rigidly attached to the hub. The hydrodynamic added mass $[\mathbf{M}_H]$ and damping matrices $[\mathbf{C}_H]$ are superimposed on to the structural mass $[\mathbf{M}]$ and damping $[\mathbf{C}]$ matrices via the use of user-defined hydroelastic elements in ABAQUS Standard. Details on the form and implementation of the hydroelastic elements are given in Young (2007).

2.4. Solution procedure

For steady flow, the solution procedure involves first computing the hydrodynamic pressures P_r due to rigid-blade rotation via the BEM, which are then applied as external normal surface traction for the FEM solid model to obtain the deformed geometry. The commercial FEM code, ABAQUS/Standard, is then used to solve the equation of motion in the rotating blade-fixed coordinate system. The centrifugal $\{\mathbf{F}_{ce}\}$ and Coriolis $\{\mathbf{F}_{co}\}$ body forces are applied as element-based loads in ABAQUS/Standard. To account large elastic displacement of the flexible composite blades, which in turn change the pressure distributions, iterations are implemented between BEM and FEM solvers until the solution (thrust coefficient, propeller efficiency, and maximum displacement) converges.

For unsteady flows, the BEM is used to compute the hydrodynamic pressure due to rigid-blade rotation, as well as the hydrodynamic added mass $[\mathbf{M}_H]$ and damping matrices $[\mathbf{C}_H]$ associated with blade accelerations and velocities,

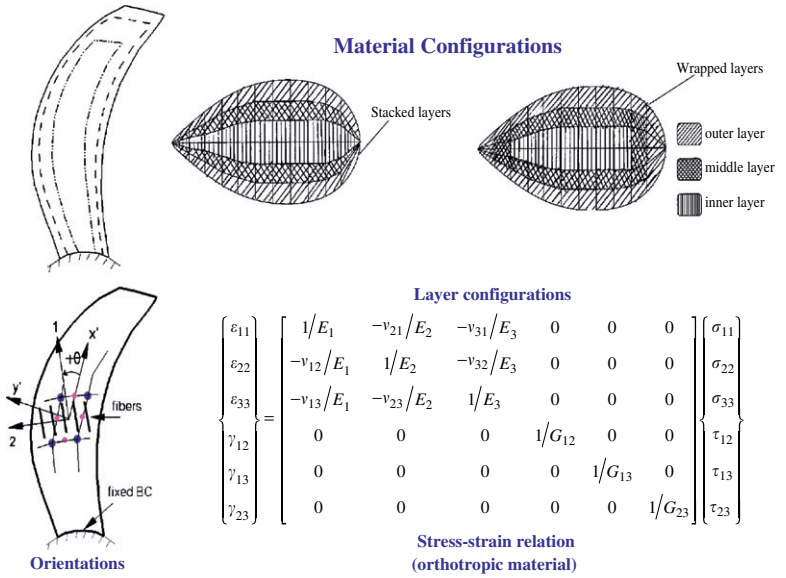

Fig. 2. Schematic drawing of the different layering configurations that can be considered by the current coupled BEM–FEM solver, along with the definition of the fiber direction with respect to the local spanwise coordinate, and stress–strain relation for a linear elastic, orthotropic material.

respectively. The added mass and hydrodynamic damping matrices are superimposed onto the structural mass and damping matrices via user-defined hydroelastic elements in ABAQUS/Standard. Similar to the case for steady flow, the centrifugal and Coriolis body forces are applied as element-based loads. The direct cyclic algorithm in ABAQUS/Standard is applied to calculate the dynamic blade response. Iterations are also implemented between the BEM and FEM solvers to account for time-dependent blade deformations. All the geometric variables (BEM influence coefficients) need to be recomputed for each BEM calculation to account for the change in blade pitch, rake, skew, and blade section on the resulting P_r, $[\mathbf{M}_H]$, and $[\mathbf{C}_H]$.

3. Validation

To validate the FEM model for a composite plate-like structure, and to determine the appropriate element type and number of elements necessary through the plate thickness, numerical results from ABAQUS are compared with the elasticity solution. For the case of a simply supported symmetric, uniform thickness 3-ply ($0^\circ/90^\circ/0^\circ$) laminate plate subject to cylindrical bending ($p = \sin \pi x/L$), the elasticity solution was obtained by Pagano (1969). The plate geometry and lamination scheme are shown in Fig. 3. The unidirectional fibrous composite has the following material properties:

$$E_1 = 172.4\,\text{GPa} = 25 \times 10^6\,\text{psi}, \quad E_2 = E_3 = 6.90\,\text{GPa} = 1 \times 10^6\,\text{psi},$$
$$G_{12} = G_{13} = 3.45\,\text{GPa} = 0.5 \times 10^6\,\text{psi}, \quad G_{23} = 1.38\,\text{GPa} = 0.2 \times 10^6\,\text{psi},$$
$$v_{12} = v_{13} = v_{23} = 0.25,$$

where 1- and 2-directions denote the direction parallel and transverse, respectively, to the fibers. E is Young's modulus, G is the shear modulus, and v is Poisson's ratio. Results are shown for the case with S(span-to-depth ratio) = 4, with L(length) = 10 m, H(thickness) = 2.5 m, B(width) = 1 m, which represents a thick plate and is a stringent test for the transverse shear.

Comparison of the axial stress σ_{11} distribution at the mid-span, transverse shear stress σ_{13} distribution at the ends, and vertical displacement u_z distribution along the bottom edge in the global system coordinates are shown in Figs. 4, 5, and 6, respectively.

Three different types of elements in ABAQUS (2004) are tested: S8R (8-noded shell elements with reduced integration), SC8R (8-noded continuum shell elements with reduced integration), and C3D20R (20-noded continuum solid elements with reduced integration). The notation "stacked n" implies $n/3$ elements per ply. The S8R elements only discretize the reference surface and have six degrees of freedom (three displacement components and three rotational

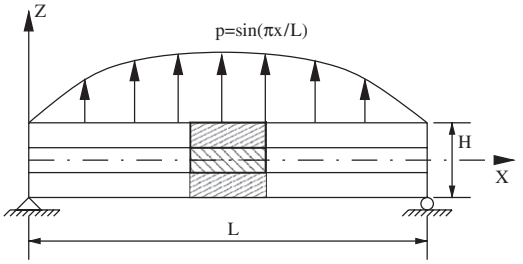

Fig. 3. Geometry and lamination scheme of a simply supported 3-ply plate subject to cylindrical bending.

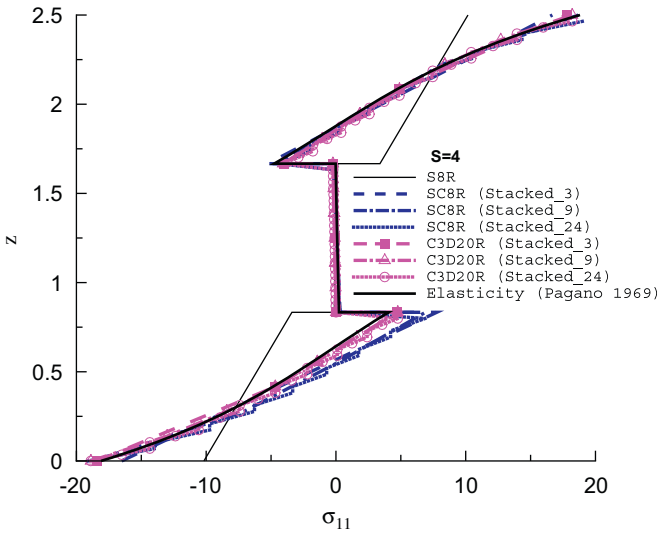

Fig. 4. Axial stress (σ_{11}) distribution at the mid-span of the simply supported composite plate. $S = 4$ denotes the span-to-depth ratio of the plate.

components) per node, but only five of the degrees of freedom are associated with stiffness. The SC8R continuum shell elements and the C3D20R continuum solid elements discretize the entire 3-D volume and have only displacement degrees of freedom. Thus, from a modeling point of view, continuum shell elements are similar to continuum solid elements, but their kinematic and constitutive behavior is similar to conventional shell elements. Continuum shell elements employ first-order layer-wise composite theory, and may be preferred over conventional shell elements because they can be stacked to provide more refined through-thickness response and allow two-sided contact with changes in the thickness (ABAQUS, 2004).

For the S8R element model, the composite shell section option is used to define the composite layers, and a five-point Simpson's rule is applied for integration in the thickness direction for each layer. The transverse shear stresses are computed by matching the elastic strain energy with the associated shear deformation of the shell section with that based on piecewise quadratic variation of the transverse shear stress across the section (ABAQUS, 2004). For the SC8R element model, either one (stacked 3) or three (stacked 9) elements are stacked in the thickness direction for each ply, and a three-point Simpson's rule is used in the thickness direction for each element. The transverse shear stress is assumed to be constant for each element and is obtained by dividing the corresponding section force over the section thickness. For the C3D20R element model, all the stress components are computed based on the constitutive behavior.

The S8R element model is able to capture the zero shear stress at the surface of the plate, but is not able to capture the stress distributions and displacements accurately due to the first-order shear deformation theory adopted for the S8R shell element. The same is true for the SC8R element model with only 1 element per material layer. As the number of SC8R elements per material layer increases, the numerical results approach the elasticity solution. However, even with 8 elements per ply (SC8R stacked 24), the displacements predicted by the SC8R model is still noticeably higher than the elasticity solution. The transverse shear stress is non-zero at the free surface for the C3D20R element model. This is because the transverse shear stresses are obtained directly from the displacement field instead of from equilibrium calculation. As the

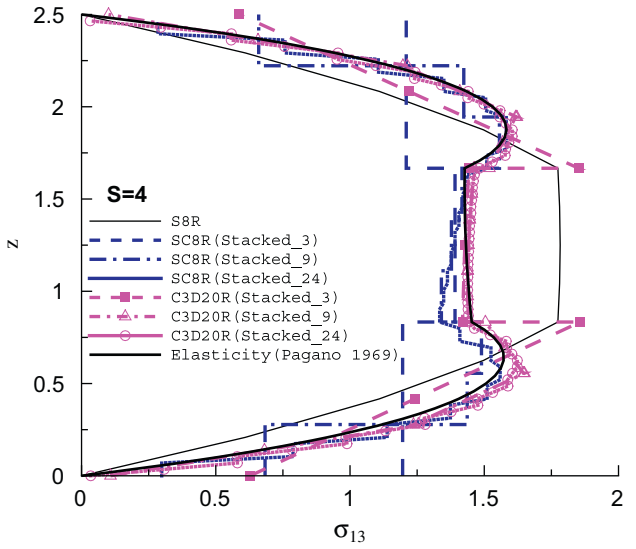

Fig. 5. Transverse shear stress (σ_{13}) distribution at supports of the simply supported composite plate. $S = 4$ denotes the span-to-depth ratio of the plate.

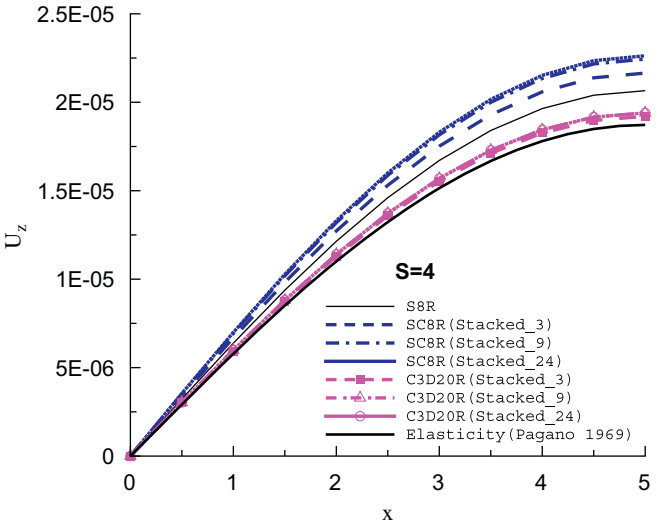

Fig. 6. Vertical deflections (u_z) distribution at the mid-span of the simply supported composite plate. $S = 4$ denotes the span-to-depth ratio of the plate.

number of C3D20R elements per material layer increases, the numerical results approach the elasticity solution faster than the SC8R element model. Moreover, the results indicate that even with only one C3D20R element per material layer, the model is able to capture reasonably well the stress distributions and displacements. Additional validation studies by the author have shown that for thinner plates (e.g. $S = 10$), which are more representative of typical propeller blades, one C3D20R element per material layer is sufficient to capture the stress distributions and deflections.

4. Results and discussions

To validate the coupled BEM/FEM method, numerical predictions are compared with experimental measurements for two composite propellers tested at the 0.9144 m (36 in) water tunnel at the Naval Surface Warfare Center, Carderock

Division (NSWCCD). The propellers were manufactured by A.I.R. Fertigung-Technologie GmbH and designed in cooperation with the NSWCCD. Details regarding the design procedure and manufacturing process can be found in Chen et al. (2006).

The geometry of the two propellers are shown in the top right-hand corners of Figs. 7 and 8, and are given in Tables 1 and 2. Both propellers are made of carbon fiber composites. Propeller 5471 was designed to be a relatively rigid composite, and it has a soft outer layer and a stiff inner core; propeller 5479 was designed to be a relatively flexible composite, and it has two soft outer layers and a stiff inner core. Propeller 5479 was designed to de-pitch near the tip to reduce the load and improve the propeller efficiency. The mechanical properties and thickness distribution of the material layers for both propellers can be obtained from A.I.R. Fertigung-Technologie GmbH. The material orientation vectors of the two propellers are shown in Figs. 9 and 10. The local 1-direction corresponds to the direction parallel to the fibers, and is approximately aligned with the spanwise direction; the local 2-direction corresponds to the direction transverse to the fibers, and is approximately aligned with the flow direction. Both propellers are 2 feet in diameter, and the design conditions in open water flow are as follows: $J = V/nD = 0.66$, $n = 909$ rpm, and $K_T = T/\rho n^2 D^4 = 0.2$. V is the propeller advance velocity, and T is the propeller thrust.

The BEM models are generated using 50 (chordwise) $\times 20$ (spanwise) constant strength surface panels per blade. The FEM models are generated using quadratic continuum (C3D20R and C3D15) solid volumetric elements. For propeller 5471, 57 elements are used in the spanwise direction, 19 elements in the chordwise direction, and 4 elements in the thickness direction. For propeller 5479, 60 elements are used in the spanwise direction, 19 elements in the chordwise direction, and 12 elements in the thickness direction. It should be noted that although the coupled BEM–FEM solver is able to predict the transient behavior of flexible composite propellers, only steady (spatially uniform) results under open water conditions are shown in this paper.

Comparisons of the predicted and measured thrust ($K_T = T/\rho n^2 D^4$), torque ($K_Q = Q/\rho n^2 D^5$), and efficiency ($\eta = (K_T/K_Q)(J/2\pi)$) coefficients for propellers 5471 and 5479, respectively, in open water at $n = 909$ rpm and 454 rpm are shown in Figs. 7 and 8. The numerical predictions corresponding to the undeformed propeller geometry, or the rigid-blade response, are also shown in Figs. 7 and 8. The deformation patterns (magnified ten times) of propeller 5471 and 5479 are shown in Figs. 9 and 10, respectively. Comparisons of the predicted and measured changes in rake and pitch angle at the blade tip as a function of the thrust T for both propellers are shown in Fig. 11. It should be noted that,

Table 1
Geometry of propeller 5471

r/R	P/D	RK/D	SK	C/D	f_0/C	τ_0/D
0.2000	44.8225	0.0002	−0.0262	0.1250	0.0004	0.0423
0.2400	45.0068	0.0049	−2.7667	0.1307	0.0004	0.0321
0.2800	45.1733	0.0103	−4.9752	0.1357	0.0208	0.0295
0.3200	43.7502	0.0150	−6.3609	0.1400	0.0319	0.0282
0.3600	41.7228	0.0196	−7.2099	0.1436	0.0372	0.0268
0.4000	39.6825	0.0241	−7.6245	0.1465	0.0395	0.0254
0.4400	37.6254	0.0284	−7.6931	0.1486	0.0405	0.0239
0.4800	35.4742	0.0326	−7.4736	0.1500	0.0408	0.0224
0.5200	33.3262	0.0367	−6.9860	0.1506	0.0402	0.0209
0.5600	31.2005	0.0407	−6.2669	0.1504	0.0389	0.0194
0.6000	29.0976	0.0445	−5.3331	0.1494	0.0370	0.0180
0.6400	27.0588	0.0482	−4.2178	0.1475	0.0352	0.0167
0.6800	25.0725	0.0517	−2.9333	0.1447	0.0332	0.0154
0.7200	23.1440	0.0550	−1.4915	0.1410	0.0310	0.0142
0.7600	21.2575	0.0581	0.0906	0.1363	0.0288	0.0132
0.8000	19.4027	0.0610	1.8029	0.1306	0.0264	0.0121
0.8400	17.5789	0.0636	3.6356	0.1239	0.0239	0.0112
0.8800	15.7972	0.0659	5.5837	0.1161	0.0208	0.0103
0.9200	14.0321	0.0678	7.6338	0.1072	0.0170	0.0095
0.9600	12.3191	0.0692	9.7821	0.0970	0.0127	0.0086
1.0001	10.5472	0.0703	12.1396	0.0732	0.0067	0.0066

Six blades, NACA 16 thickness and $a = 0.8$ camber distribution.
The variables from left to right on the first row of the table indicate the radius, pitch to diameter ratio, rake to diameter ratio, skew angle in degrees, chord to diameter ratio, maximum camber to chord ratio, and maximum thickness to chord ratio of each blade section.

Table 2
Geometry of propeller 5479

r/R	P/D	RK/D	SK	C/D	f_0/C	τ_0/D
0.2000	44.8310	0.0001	−0.0486	0.1257	0.0005	0.0423
0.2400	45.0731	0.0049	−2.8152	0.1313	0.0000	0.0321
0.2800	45.0148	0.0100	−4.9540	0.1362	0.0183	0.0295
0.3200	43.9097	0.0150	−6.4305	0.1405	0.0313	0.0282
0.3600	42.0917	0.0197	−7.3247	0.1441	0.0371	0.0268
0.4000	40.1489	0.0243	−7.7774	0.1470	0.0396	0.0254
0.4400	38.2385	0.0288	−7.8776	0.1491	0.0407	0.0239
0.4800	36.2507	0.0333	−7.6902	0.1506	0.0410	0.0224
0.5200	34.2324	0.0378	−7.2412	0.1512	0.0404	0.0209
0.5600	32.2622	0.0422	−6.5593	0.1510	0.0391	0.0194
0.6000	30.3752	0.0466	−5.6656	0.1500	0.0373	0.0180
0.6400	28.5523	0.0509	−4.5869	0.1481	0.0353	0.0167
0.6800	26.7838	0.0553	−3.3442	0.1453	0.0334	0.0154
0.7200	25.0692	0.0596	−1.9507	0.1416	0.0312	0.0142
0.7600	23.3993	0.0639	−0.4176	0.1369	0.0290	0.0132
0.8000	21.7509	0.0682	1.2431	0.1312	0.0266	0.0121
0.8400	20.1032	0.0725	3.0241	0.1244	0.0241	0.0112
0.8800	18.4243	0.0767	4.9186	0.1164	0.0211	0.0103
0.9200	16.6946	0.0806	6.9210	0.1073	0.0175	0.0095
0.9600	14.9333	0.0844	9.0190	0.0971	0.0130	0.0086
1.0000	13.0273	0.0875	11.3859	0.0714	0.0070	0.0063

Six blades, NACA 16 thickness and $a = 0.8$ camber distribution.
The variables from left to right on the first row of the table indicate the radius, pitch to diameter ratio, rake to diameter ratio, skew angle in degrees, chord to diameter ratio, maximum camber to chord ratio, and maximum thickness to chord ratio of each blade section.

although propeller 5471 did undergo a small change in pitch, the magnitude was within the error of the measurement technique (which involves the use of lasers to track the deformation at the tip of the blade while rotating in water), and thus the measured change in pitch angle at the blade tip for propeller 5471 is not shown in Fig. 11.

As shown in the figures, the numerical predictions compare well with experimental measurements. As the advance coefficient J decreases, the effective angle of attack increases. Consequently, the load coefficients and blade deformations also increase. Due to the higher pressures on the face (pressure) side, the blade tends to bend toward the upstream direction, which decreases the rake (defined positive for bending of the blade about the z-axis toward the downstream direction). The deformation increases toward the tip due to the cantilever-like behavior of the blade. The flexible composite propeller (5479) was designed to de-pitch, i.e. the undeformed (unloaded) blade was designed to have a higher pitch near the tip (than its rigid counterpart, propeller 5471) to account for the expected decrease in pitch under hydrodynamic load by utilizing the elastic bending–twisting coupling effect of orthotropic composites. Hence, when the flexible blades de-pitch to approach the intended design values, the thrust and torque coefficients decrease due to the unloading near the tip, and the propeller efficiencies increase because the reduction in torque is higher than the reduction in thrust.

As shown in Figs. 7–11, the propellers performed as expected, i.e. the pitch angle, rake, thrust coefficient, and torque coefficient decrease, and the propeller efficiency increases due to blade deformation. In general, the predicted changes in rake and pitch angle at the blade tip for both propellers agree well with experimental measurements. It should be emphasized again that it is difficult to accurately measure the change in rake and pitch angle at the blade tip while the propeller is rotating and undergoing elastic blade deformation at 909 rpm in the water tunnel.

Comparisons of the predicted non-dimensionalized wetted pressure distribution ($-C_p = (P_o - P)/(\frac{1}{2}\rho n^2 D^2)$) for the undeformed and deformed geometries of propellers 5471 and 5479 at the design condition are shown in Figs. 12 and 13. The corresponding von Mises stress distributions for both propellers (in the deformed configuration) are shown in Figs. 14 and 15.

As shown in Figs. 12 and 13, propeller 5479 undergoes a greater change in pressure distribution in the tip region than propeller 5471 due to larger elastic blade deformation, which is consistent with the deformation patterns. As shown in Figs. 14 and 15, more differences can be observed in the predicted von Mises stress distributions due to the differences

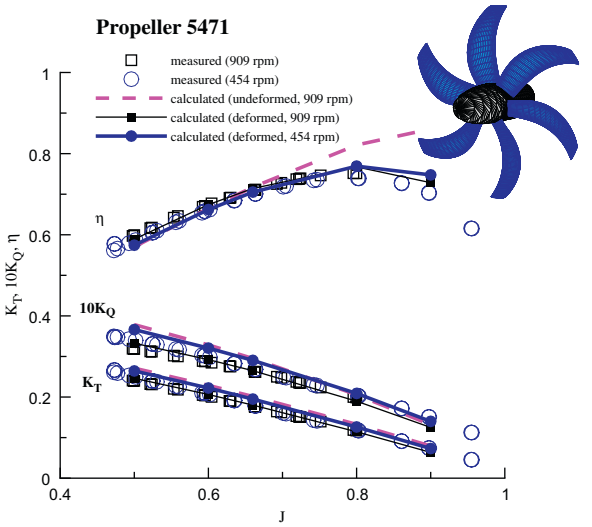

Fig. 7. Comparison of the predicted and measured open water subcavitating load coefficients for propeller 5471. The discretized geometry of the propeller is shown in the inset on the top, right-hand corner.

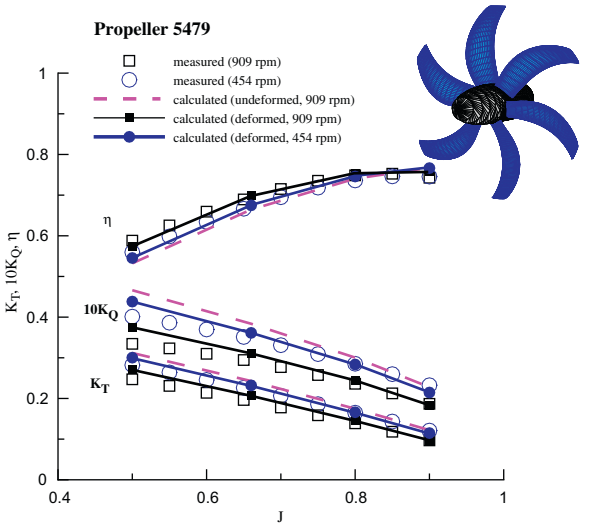

Fig. 8. Comparison of the predicted and measured open water subcavitating load coefficients for propeller 5479. The discretized geometry of the propeller is shown in the inset on the top, right-hand corner.

in material composition. Propeller 5471 develops higher stresses on the mid-chord section on the back (suction) side and along the trailing edge on the face (pressure) side of the blade. Propeller 5479 develops higher stresses near the trailing edge at the face side near the root of the blade and in between the two inner layers at the root section inside the blade. The maximum predicted von Mises stress is 52 MPa for propeller 5471 and 104 MPa for propeller 5479, both of which are less than the tensile strength of the material. It is expected that propeller 5479 develops higher stress due to larger deformations and softer material properties. It is also expected that propeller 5479 develops the highest stress in between the two inner layers at the root because that is the area where the maximum moment develops, and because the large differences between the material properties of the inner layers.

Comparisons of the predicted cavitation patterns and thrust breakdown curves for the two propellers are shown in Figs. 16 and 17. Also shown in the figures are the measured cavitation number ($\sigma_n = (P_o - P_c)/(\frac{1}{2}\rho n^2 D^2)$) and thrust

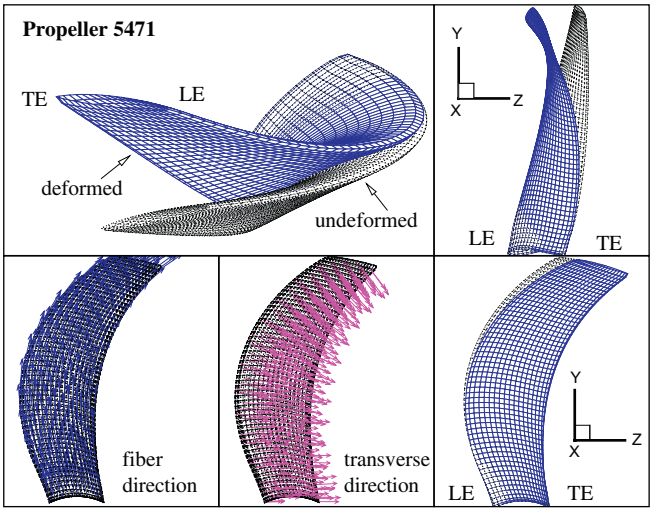

Fig. 9. Material orientation vectors and comparison of the undeformed and deformed geometries of propeller 5471 in subcavitating flow; $J = 0.66$, $n = 909$ rpm.

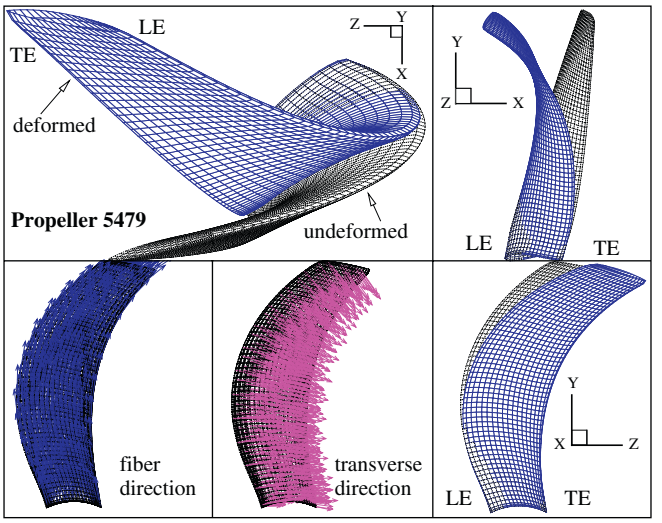

Fig. 10. Material orientation vectors and comparison of the undeformed and deformed geometries of propeller 5479 in subcavitating flow; $J = 0.66$, $n = 909$ rpm.

coefficient (K_T) when mid-chord suction side patch cavitation was first observed on the blades. The multiple experimental data points correspond to when cavitation was observed on one, two, or more blades. Although the propellers are subject to uniform inflow, cavitation inception may not necessarily occur at the same inception speed on all six blades because the cavities are unstable at inception, and because all six blades are not exactly identical due to the complex manufacturing process of composites.

Overall, the predicted cavitation numbers corresponding to first inception of mid-chord patched cavitation matched well with experimental measurements. According to the researchers who carried out the experiments at NSWCCD, the predicted mid-chord suction side cavitation pattern agrees with experimental observations. However, direct comparison of the predicted and observed cavitation patterns cannot be made because the cavitation patterns were not photographed. As shown in Figs. 16 and 17, the cavitating thrust and torque coefficients decrease, and propeller efficiencies increase due to blade deformation. Similar to the wetted performance, propeller 5479 benefits more from the

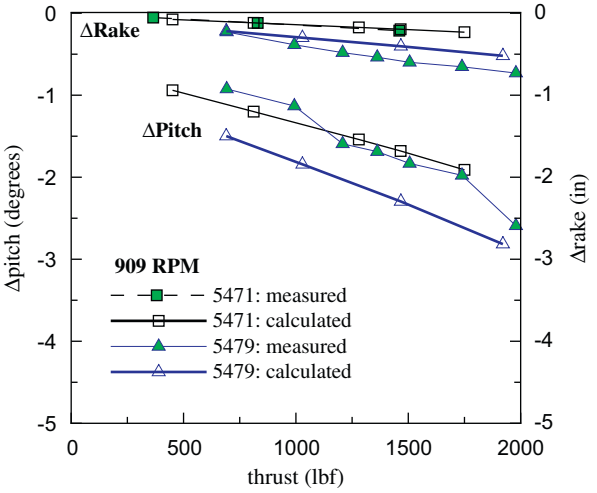

Fig. 11. Comparisons of the predicted and measured change in rake and pitch angle at the blade tip as a function of the thrust (T) for propellers 5471 and 5479 in subcavitating flow; $n = 909$ rpm.

elastic deformation than propeller 5471 (when compared to its respective undeformed performance) due to the higher change in pitch angle. The final cavitation patterns are very similar on both propellers due to similar pressure distributions.

The predicted natural frequencies in air and in water for propellers 5471 and 5479 at 909 rpm are shown in Fig. 18. Also shown in the figure are the measured fundamental ($m = 1$) frequencies in water and the predicted mode shapes. The predicted fundamental frequencies in water (123 Hz for propeller 5471 and 89 Hz for propeller 5479) agree reasonably well with the inferred fundamental frequency of approximately 91 Hz, obtained via acoustic measurements when the propellers are placed behind a wake screen. It should be noted that the natural frequencies of propeller 5479 should be slightly lower than propeller 5471 due to the use of the softer material in the outer layer, as predicted by the coupled BEM–FEM solver. The mode shapes of both propellers are approximately the same, i.e. the first mode is primarily bending and the second mode is combined bending and twisting. It is important to note that the natural frequencies are approximately 50% lower in water due to the added mass effect. The low-fundamental frequency in water suggests that the blades may be susceptible to load amplification due to near-resonant blade vibration, particularly when operating in a spatially varying wake.

It is important to mention here that both experimental and numerical studies showed that the rigid (5471) and flexible (5479) composite propeller pair did not meet the design criterion that requires them to produce the same thrust and efficiency under the design operating condition ($J = 0.66$ at $n = 909$), as shown in Fig. 19. The results showed that propeller 5471 is not really rigid (i.e. more flexible than intended), which caused the blades to undergo bending (which should not affect the propeller performance) and a slight twisting (which does affect the propeller performance due to change in pitch), as shown in Fig. 9. Consequently, under design conditions, the efficiency of propeller 5471 in the deformed configuration is higher than that in the undeformed configuration due to unloading caused by small changes in pitch. On the other hand, propeller 5479 is more rigid than intended, as evident by the small change in pitch shown in Fig. 11. Although propeller 5479 undergoes more deformation than propeller 5471, it did not deformed as much as intended by the design. Consequently, the deformed geometry of propeller 5479 did not match that of the design, which resulted in a slightly smaller (deformed) efficiency increased compared to intended. Hence, as depicted in Fig. 19, both numerical and experimental results show that propellers 5471 and 5479 did not produce the same thrust and efficiency under the design condition ($J = 0.66$ at $n = 909$ rpm). Moreover, the efficiency of propeller 5479 is actually less than that of propeller 5471 for $J < 0.85$. This unintended performance is due primarily to the difficulties in the design and manufacturing processes. It is important to note that the author was not involved in the design and testing of the composite propellers, and the coupled BEM–FEM solver was not available at the time of the design. Nevertheless, although both propellers 5471 and 5479 did not perform exactly according to design, the results can still be used to validate the numerical model, which is the objective of this work. From the numerical perspective, it is actually encouraging to see the good agreement between numerical predictions and experimental

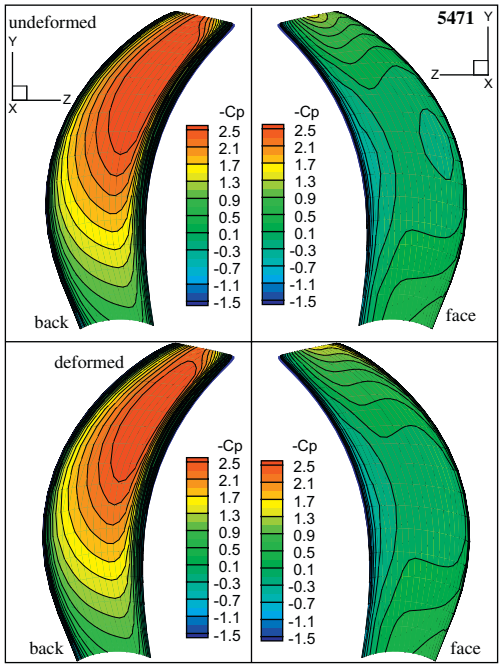

Fig. 12. Predicted wetted pressure distributions for propeller 5471 in the undeformed and deformed configuration; $J = 0.66$, $n = 909$ rpm.

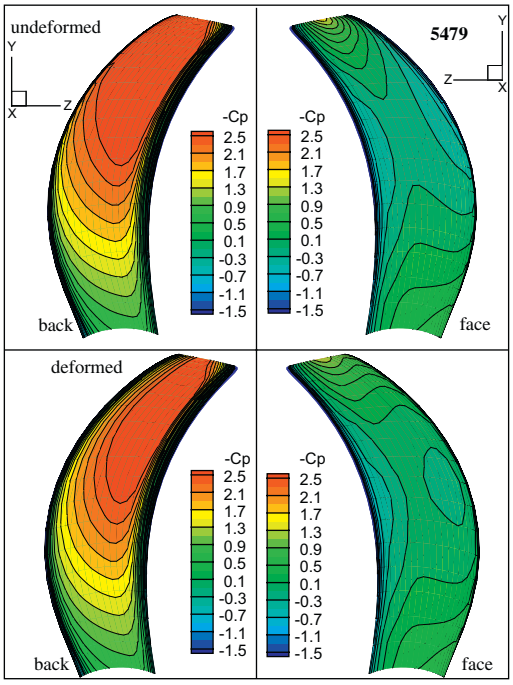

Fig. 13. Predicted wetted pressure distributions for propeller 5479 in the undeformed and deformed configuration; $J = 0.66$, $n = 909$ rpm.

measurements, and to discern the source of the deviation from the intended and observed performances. The results also suggest that the coupled BEM–FEM solver can be used to improve the design of flexible self-twisting composite propellers.

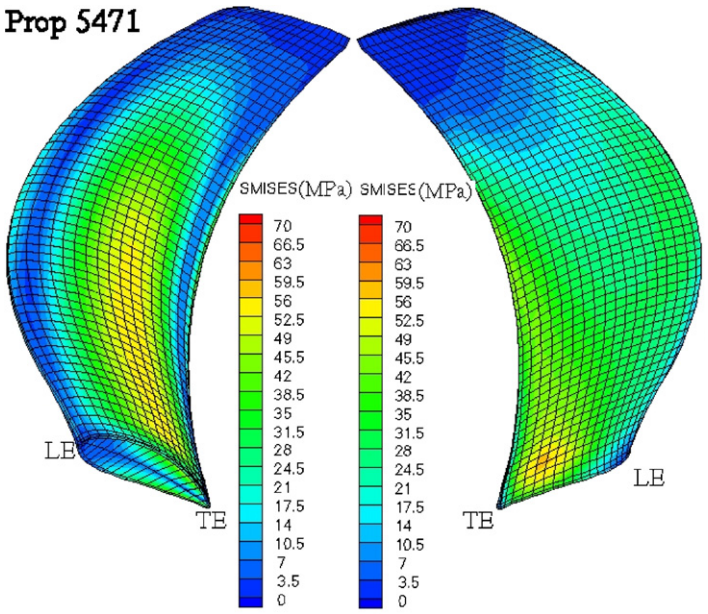

Fig. 14. Predicted fully wetted von Mises stress distributions for propeller 5471; $J = 0.66$, $n = 909$ rpm.

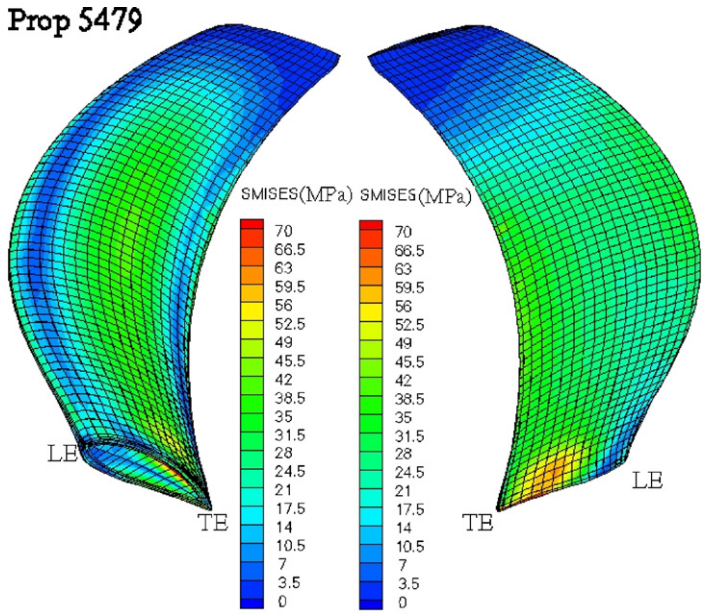

Fig. 15. Predicted fully wetted von Mises stress distributions for propeller 5479; $J = 0.66$, $n = 909$ rpm.

5. Conclusions

A general methodology is presented for the fluid–structure interaction analysis of flexible composite marine propellers subject to hydrodynamic and inertial loads, including the effect of unsteady cavitation. The method is able to predict the hydrodynamic blade loads, cavitation patterns, stress distributions, and deflection patterns of flexible composite propellers.

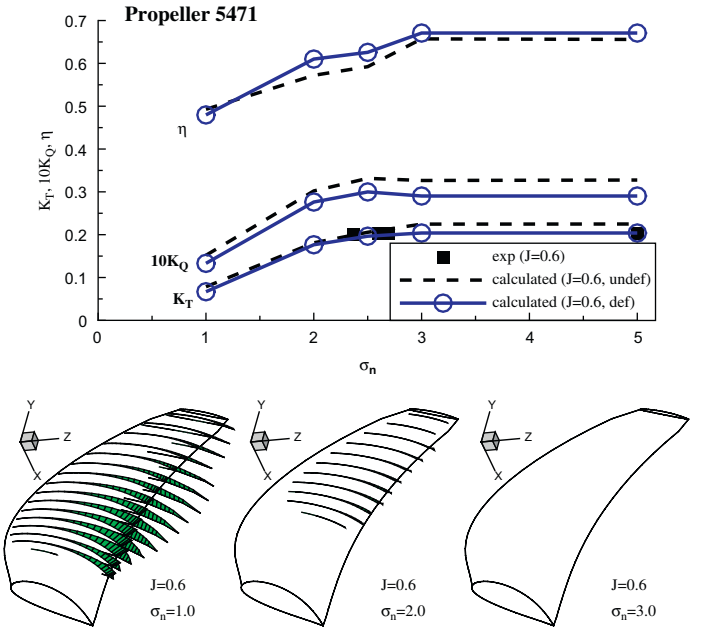

Fig. 16. Cavity breakdown curves and cavitation patterns for propeller 5471. Also shown are the measured values (exp) when mid-chord suction side patch cavitation was first observed; $J = 0.6$, $n = 909$ rpm.

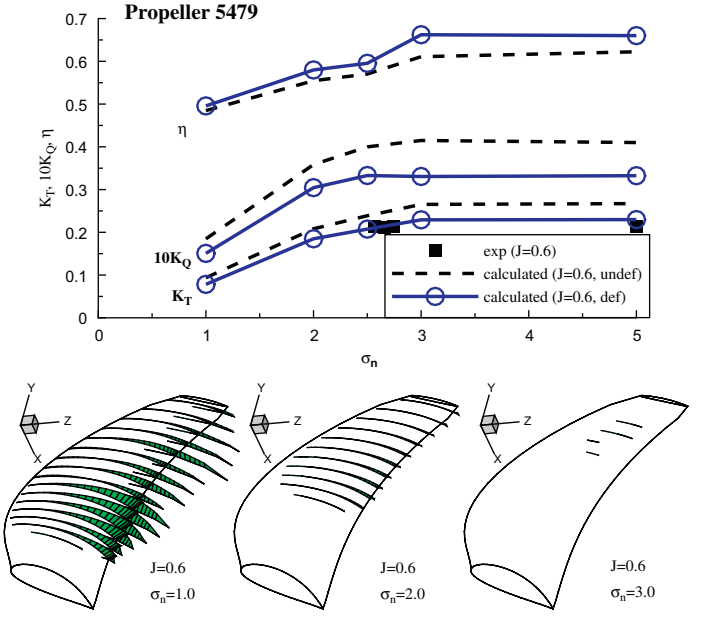

Fig. 17. Cavity breakdown curves and cavitation patterns for propeller 5479. Also shown are the measured values (exp) when mid-chord suction side patch cavitation was first observed; $J = 0.6$, $n = 909$ rpm.

The FEM model is validated by comparing the numerical results with the analytical elasticity solution for a simply supported composite plate subject to cylindrical bending. The validation study suggests that stacked quadratic continuum solid elements can better capture the structural behavior of composite plates than conventional and continuum shell elements.

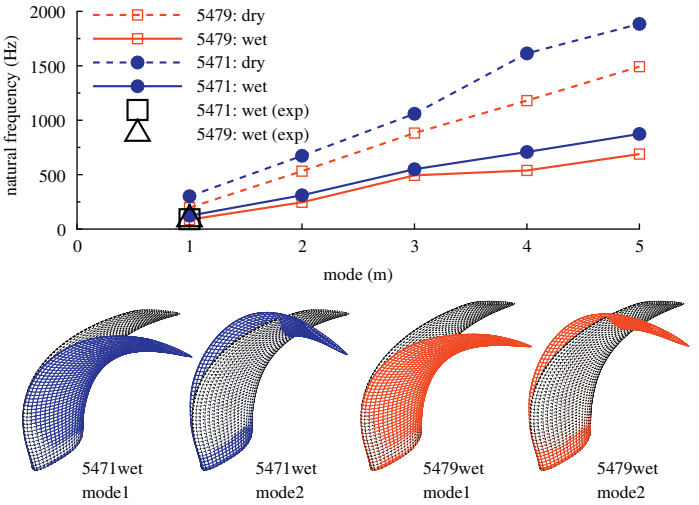

Fig. 18. Predicted and measured natural frequencies and mode shapes for propellers 5471 and 5479; $n = 909$ rpm.

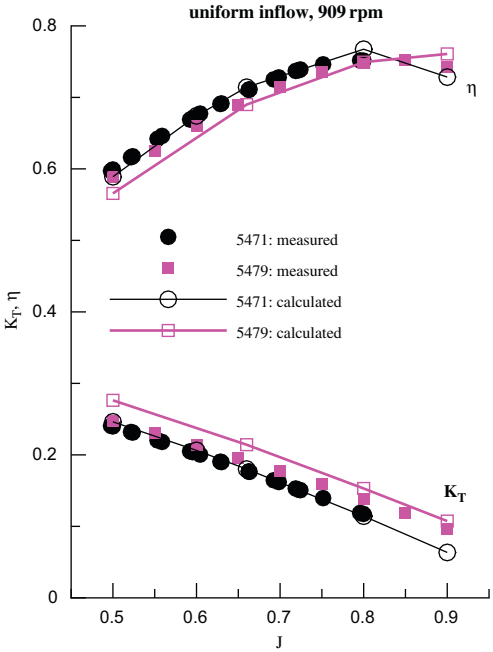

Fig. 19. Predicted and measured performance of propellers 5471 and 5479; $n = 909$ rpm.

Experimental validation studies are presented for two composite propellers tested at the NSWCCD. The predicted performance curves, blade tip deflections, cavitation inception speeds, cavitation patterns, and fundamental frequencies in water agreed well with experimental measurements and observations.

The following conclusions can be drawn from the studies presented in this paper.

(i) It is important to include the effect of fluid–structure interaction in the analysis of flexible composite propellers because the blade deformation changes the local flow field, which in turn changes the fluid pressure distributions, cavitation patterns, and resulting propeller efficiencies.

(ii) The effect of fluid–structure interaction is also important when calculating the fundamental frequencies of composite marine propellers, which can be significantly reduced due to the added mass effect.

(iii) Elastic deformations can lead to changes in the blade pitch angle (the angle that the chord of the blade section makes with the plane of rotation), rake (the distance the blade bends toward the downstream direction), and skew (the angle that the blade bends toward its trailing edge), all of which affect the propeller performance.
(iv) The stress distributions and deflection patterns depend highly on the material composition and layering sequence. Thus, it is important to investigate the hydroelastic response of flexible composite propellers to determine the performance envelope and to avoid material failure.
(v) Flexible composite propellers may be subject to resonant blade vibration and fatigue problems due to the decreased fundamental frequency as a result of the reduced mass and increased material flexibility.

It should be noted that it is also possible to change the inception speed, volume, and pattern of cavitation by changing the pressure distributions through passive hydroelastic tailoring of the blade deformations. Ideally, at the design operating condition ($J = J_{\text{design}}$, where J_{design} is the design advance coefficient), the deformed blade geometry should match that of an optimal rigid blade geometry; at off-design conditions, the bending–twisting coupling effect of composites should allow the pitch near the tip of the deformed flexible blade to be lower than its rigid counterpart at $J < J_{\text{design}}$ (over-pitch situations), and to be higher than its rigid counter at $J > J_{\text{design}}$ (under-pitch situations). This automatic adjustment is desired and is possible, because at $J < J_{\text{design}}$ the blades undergo more deformation and thus more decrease in pitch due to the higher load, which allows the deformed pitch of the flexible blade to be lower than its counterpart. The opposite should be true at $J > J_{\text{design}}$. Thus, the efficiency of the flexible composite propeller should match that of its rigid counterpart at the design condition ($J = J_{\text{design}}$), and should be higher than its rigid counterpart at off-design conditions ($J < J_{\text{design}}$ and $J > J_{\text{design}}$). The de-pitching of the blades near the tip should also help to delay cavitation inception. Moreover, improvements in propeller efficiency and cavitation characteristics of a properly designed flexible composite propeller should be even more prominent in spatially varying flows due to the instantaneous benefit from the bending–twisting coupling when the blades pass through wake deficit regions. In addition, the automatic pitch adjustment should help to reduce load variations and reduce the strength of the tip vortex, which can further enhance the propeller performance in a spatially varying wake. All of these are very important advantages that cannot be achieved using isotropic metallic materials, which do not exhibit bending–twisting coupling behavior, and thus the potential twisting is limited since it is dependent on geometric nonlinearity (e.g. the leading edge thicker than the trailing edge, high skew, rake, and/or pitch) from bending deformation.

The results from this study suggest that a fluid–structure interaction analysis method, such as that presented in this paper, should be used in the design of flexible composite propellers to properly account for the nonlinear load-dependent bending and twisting deformations. Nevertheless, more work is still necessary in order to fully exploit the potential of passive hydroelastic tailoring of marine propellers, including unsteady experimental validation studies, and investigation of potential failure mechanisms of laminated composites.

Acknowledgments

Support for this research was provided by Naval Surface Warfare Center Carderock Division (Contract no. N000167-05-M-0100) and Office of Naval Research (Contract no. N00014-05-1-0694). The authors would like to thank Dr Ki-Han Kim of ONR, and Dr Ben Chen, Dr Richard Szwerc, and Mr Thad Michael of NSWCCD for their support and for providing the experimental data.

References

ABAQUS, 2004. ABAQUS Version 6.5 Documentation. ABAQUS, Inc., 1080 Main Street, Pawtucket, RI 02860, USA.

Anon, 2003. World's largest composite propeller successfully completes sea trials. The Naval Architect 16.

Ashkenazi, Y., Gol'fman, I., Rezhkov, L., Sidorov, N., 1974. Glass-Fiber-Reinforced Plastic Parts in Ship Machinery. Sudostroyenniye Publishing House, Leningard.

Brillouin, M., 1911. Les surfaces de glissement de Helmholtz et la resistance des fluides. Annales de Chimie and de Physique 23, 145–230.

Chen, B., Neely, S., Michael, T., Gowing, S., Szwerc, R., Buchler, D., Schult, R., 2006. Design, fabrication and testing of pitch-adapting (flexible) composite propellers. In: The SNAME Propeller/Shafting Symposium. Williamsburg, VA, USA.

Choi, J., 2000. Vortical inflow—propeller interaction using unsteady three-dimensional Euler solver. Ph.D. Thesis, Department of Civil Engineering, The University of Texas at Austin, TX, USA.

Greeley, D., Kerwin, J., 1982. Numerical methods for propeller design and analysis in steady flow. Transactions, Society of Naval Architects and Marine Engineers 90, 415–453.

Hashin, Z., 1980. Failure criteria for unidirectional fiber composites. Journal of Applied Mechanics 47, 329–334.

Kane, C., Dow, R., 1994. Marine propulsors design in fibre reinforced plastics. Journal of Defense Science 4, 301–308.
Kerwin, J., Lee, C.-S., 1978. Prediction of steady and unsteady marine propeller performance by numerical lifting-surface theory. Transactions, Society of Naval Architects and Marine Engineers 86, 218–253.
Kinnas, S., Fine, N., August 1992. A nonlinear boundary element method for the analysis of unsteady propeller sheet cavitation. In: Nineteenth Symposium on Naval Hydrodynamics, Seoul, Korea, pp. 717–737.
Kinnas, S., Fine, N., September 1993. A numerical nonlinear analysis of the flow around two- and three-dimensional partially cavitating hydrofoils. Journal of Fluid Mechanics 254, 151–181.
Kinnas, S., Young, Y., 2003. Modeling of cavitating or ventilated flows using bem. International Journal of Numerical Methods for Heat & Fluid Flow 13 (6), 672–697.
Kinnas, S., Choi, J., Lee, H., Young, J., 2000. Numerical cavitation tunnel. In: NCT50, International Conference on Propeller Cavitation, Newcastle-upon-Tyne, England.
Lee, Y.-J., Lin, C.-C., 2004. Optimized design of composite propeller. Mechanics of Advanced Materials and Structures 11 (1), 17–30.
Lin, G., 1991a. Comparative stress-deflection analyses of a thick-shell composite propeller blade. Technical Report, David Taylor Research Center, DTRC/SHD-1373-01.
Lin, G., 1991b. Three-dimensional stress analyses of a fiber-reinforced composite thruster blade. In: Symposium on Propellers/Shafting, Society of Naval Architects and Marine Engineers, Virginia Beach, VA, USA.
Lin, C., Lee, Y., 2004. Stacking sequence optimization of laminated composite structures using genetic algorithm with local improvement. Composite Structures 63 (3–4), 339–345.
Lin, H., Lin, J., 1996. Nonlinear hydroelastic behavior of propellers using a finite element method and lifting surface theory. Journal of Marine Science and Technology 1 (2), 114–124.
Lin, H., Lin, J., 1997. Effect of stacking sequence on the hydroelastic behavior of composite propeller blades. In: Eleventh International Conference on Composite Materials, Australian Composite Structures Society, Gold Coast, Australia.
Lin, H., Lin, J., 2005. Strength evaluations of a composite marine propeller blade. Journal of Reinforced Plastics and Composites 17, 1791–1807.
Mouritz, A., Gellert, E., Burchill, P., Challis, K., 2001. Review of advanced composite structures for naval ships and submarines. Composite Structures 53, 21–41.
Pagano, N., July 1969. Exact solution for composite laminates in cylindrical bending. Journal of Composite Materials 3 (2), 398–411.
Pegg, R., Reyes, H., 1987. Progress in naval composites. Advanced Materials and Processes 3, 35–40.
Searle, T., Shot, D., 1994. Are composite propellers the way forward for small boats. Materials World: The Journal of the Institute of Materials 2 (2), 69–70.
Villat, H., 1914. Sur la validité des solutions de certain problème d' hydrodynamique. Journal de Mathématiques 6 (10), 231–290.
Womack, S., 1993. Carbon propeller allows ships to go softly softly. Engineer 276, 30.
Young, Y., 2007. Time-dependent hydroelastic analysis of cavitating propulsors. Journal of Fluids and Structures 23 (2), 269–295.
Young, Y., Kinnas, S., 2001. A BEM for the prediction of unsteady midchord face and/or back propeller cavitation. ASME Journal of Fluids Engineering 123, 311–319.
Young, Y., Kinnas, S., 2003a. Analysis of supercavitating and surface-piercing propeller flows via bem. Journal of Computational Mechanics 32 (5–6), 269–280.
Young, Y., Kinnas, S., 2003b. Numerical modeling of supercavitating propeller flows. Journal of Ship Research 47 (1), 48–62.
Young, Y., Kinnas, S., 2004. Performance prediction of surface-piercing propellers. Journal of Ship Research 48 (4), 288–304.